Optics & Laser Technology 183 (2025) 112300

Contents lists available at ScienceDirect

Optics and Laser Technology

journal homepage: www.elsevier.com/locate/optlastec

Full length article

Coded aperture imaging using non-linear Lucy-Richardson algorithm

Agnes Pristy Ignatius Xavier [a,b,*], Tauno Kahro [a], Shivasubramanian Gopinath [a], Vipin Tiwari [a], Daniel Smith [c], Aarne Kasikov [a], Helle-Mai Piirsoo [a], Soon Hock Ng [c], Aravind Simon John Francis Rajeswary [a], Jitraporn Vongsvivut [d], Aile Tamm [a], Kaupo Kukli [a], Saulius Juodkazis [c,e], Joseph Rosen [b], Vijayakumar Anand [a,c]

[a] Institute of Physics, University of Tartu, W. Ostwaldi 1, 50411 Tartu, Estonia
[b] School of Electrical and Computer Engineering, Ben Gurion University of the Negev, P.O. Box 653, Beer-Sheva 8410501, Israel
[c] Optical Sciences Center and ARC Training Centre in Surface Engineering for Advanced Materials (SEAM), School of Science, Computing and Engineering Technologies, Optical Sciences Center, Swinburne University of Technology, Hawthorn, Melbourne, VIC 3122, Australia
[d] Infrared Microspectroscopy (IRM) Beamline, ANSTO—Australian Synchrotron, Clayton, VIC 3168, Australia
[e] Tokyo Tech World Research Hub Initiative (WRHI), School of Materials and Chemical Technology, Tokyo Institute of Technology, 2-12-1, Ookayama, Meguro-ku, Tokyo 152-8550, Japan

ARTICLE INFO

Keywords:
Coded aperture imaging
Infrared imaging
Computational imaging
Non-linear Lucy-Richardson algorithm
Diffractive optics
Photolithography

ABSTRACT

Imaging involves the process of recording and reproducing images as close to reality as possible, encompassing both direct and indirect approaches. In direct imaging, the object is directly recorded. Coded aperture imaging (CAI) is an example of indirect imaging, that utilizes optical recording and computational reconstruction to obtain information about an object. Computational reconstruction can be achieved using different linear, non-linear, iterative, and deep learning algorithms. In this study, we proposed and demonstrated two computational reconstruction algorithms based on the non-linear Lucy-Richardson algorithm (NL-LRA), one for limited support images and another for full-view images based on entropy reduction. The efficacy of these algorithms has been validated through simulations and optical experiments carried out in visible and infrared (IR) light with different coded phase masks. The methods were also tested on a commercial IR microscope with internal Globar™ and synchrotron sources. The results obtained from the two algorithms were compared with those from their parent methods, and a notable improvement in both entropy and the convergence rate was observed. We believe the developed algorithms will drastically improve image reconstruction in incoherent imaging applications.

1. Introduction

The coded aperture imaging (CAI) technique has revolutionized the field of imaging by decreasing the reliance on advanced manufacturing technologies and materials engineering and expanding imaging technology to non-visible regions of electromagnetic spectra [1–4]. CAI converts the conventional single-step optical imaging process into a two-step imaging process consisting of optical recording and computational reconstruction [5]. Even though the two-step imaging process resembles the imaging process of digital holography, the requirements and outcomes are quite different [6]. In digital holography, a two-step process is carried out to obtain additional information about the object, such as phase information in coherent and 3D location information in incoherent systems [6–8]. In the optical recording process, instead of recording the image of an object, a digital hologram in which the 3D location information (incoherent) or the phase information (coherent) is recorded. In the computational reconstruction process, the digital hologram is processed to obtain additional phase or 3D location information. The computational process can vary from numerical backpropagation of the hologram to various filtering methods. In CAI, the two-step process enables imaging within the boundaries of the imaging characteristics of lens-based direct imaging systems but without lenses. In CAI, the point spread function (PSF) is recorded once using a point object. An object is then optically recorded, and the response-to-object intensity is processed with the PSF on the computer to reconstruct a 2D image of the object. In CAI, the end goal is to achieve the

* Corresponding author.
E-mail address: agnes.pristy.ignatius.xavier@ut.ee (A.P. Ignatius Xavier).

https://doi.org/10.1016/j.optlastec.2024.112300
Received 15 July 2024; Received in revised form 28 October 2024; Accepted 8 December 2024
Available online 16 December 2024

optimal qualities of the image obtained through direct imaging without a lens but with a two-step optical-computational method. Another important difference between CAI and digital holography is the ratio between the optical load and computational load in the imaging process, which is high for digital holography and low for CAI.

Research on the CAI has focused on two main directions, namely, finding the optimal coded mask (CM) and the reconstruction method. Different CMs, such as the uniformly redundant array (URA) [3,9], modified URA (MURA) [10] and Fresnel zone aperture (FZA) [11], were tested in CAI to determine the optimal imaging conditions for direct imaging methods. Different reconstruction methods have also been developed to improve the signal-to-noise ratio. While the initial studies used matched filters, improved methods such as phase-only filters [12], inverse filters [13], Wiener deconvolution (WD) [14], and the Lucy-Richardson algorithm (LRA) [15,16] were subsequently developed to improve the signal-to-noise ratio (SNR) of image reconstruction in CAI. In all the previous studies mentioned above, the goal of CAI was to reach the optimal limits of the direct imaging system. However, CAI was found to be useful for other applications, such as spectral imaging and sensing [17,18].

In 2017, CAI was extended for 3D imaging of objects with incoherent light for the first time [19]. In addition to 3D imaging, CAI can be useful for several other applications such as image resolution improvement [20], field-of-view extension [21], partial aperture imaging [22], depth-of-field engineering [23], and imaging through scattering layers [24]. During this development, it was observed that the existing reconstruction methods were not optimal for image reconstruction because multiple planes with different degrees of blur were present in the same reconstruction. Therefore, a matched filter and phase-only filter were applied to complex PSF and response-to-object intensity patterns formed from multiple recordings. The demand for recording dynamic events requires advanced computational reconstruction methods. Research in this area led to the invention of the non-linear reconstruction method (NLR) [25]. Although single-shot capability was achieved in the NLR, the SNR was still not close to that of direct imaging systems. Different computational reconstruction methods have been developed by different research groups to further improve the SNR [26,27]. The Lucy-Richardson-Rosen algorithm (LRRA) was developed and demonstrated to be a combination of the NLR and LRA and to have improved performance compared to both the LRA and NLR [28–30]. LRRA was faster than LRA by two orders of magnitude in some cases but still slower than NLR, as most of the reconstructions required at least 5 to 10 iterations. Recently, a new computational reconstruction method called incoherent non-linear deconvolution using an iterative algorithm (INDIA) was developed [31]. Any reconstruction result from existing algorithms can be improved by the INDIA. Nevertheless, the performance and convergence of INDIA depend on the input given from an existing algorithm. In [31], it was found that LRRA and WD performed the best for a wide range of CMs, so the outputs of LRRA and WD were used as inputs of INDIA.

In this study, we developed two types of the non-linear Lucy Richardson algorithm (NL-LRA) for improving reconstructions of limited support images (LSIs) and full-view images (FVIs). The LSIs have a small field of view that fills only part of the image sensor, and FVIs have a large field of view that fills the entire image sensor. For LSIs, the first type NL-LRA1 provides a better estimation than LRRA. This is achieved by applying a mask constraint within the iterative loop of LRRA. This imposes challenges not only for NL-LRA1 but also for INDIA. To address these problems and improve the reconstruction results of FVIs, a blind entropy minimization technique NL-LRA2 has been developed and added within the iterative loop of LRRA. The manuscript consists of four sections. The theory is presented in the next section. Experiments with visible, near-IR, and IR wavelengths with different types of CMs are presented and discussed in the third section. The conclusion and future perspectives are presented in the final section. A supplementary section on simulation studies and commented MATLAB codes for executing NL-LRA1 and NL-LRA2 has been provided. Recently, there has been a surge of deep learning-based imaging reconstruction methods that are beyond the scope of this study [32–34].

2. Methodology

The optical configuration is shown in Fig. 1(a). Light from a point object is modulated by a CM, and the PSF (I_{PSF}) is recorded in the first step. An object O is mounted at the same location as the point object, and the response-to-object intensity (I_O) is recorded. The I_{PSF} and I_O are processed on a computer using a computational reconstruction algorithm to reconstruct the image of the object. A point object with an amplitude of $\sqrt{I_s}$ located at $(\bar{r}_s, z_s)$ is considered. The complex amplitude reaching the CM is given as $\sqrt{I_s}C_1L\left(\frac{\bar{r}_s}{z_s}\right)Q\left(\frac{1}{z_s}\right)$, where Q is a quadratic phase function given as $Q(b) = exp\left[i\pi b\lambda^{-1}\left(x^2+y^2\right)\right]$, L is the linear phase function given as $L\left(\frac{\bar{s}}{z}\right) = exp\left[i2\pi(\lambda z)^{-1}\left(s_x x + s_y y\right)\right]$ and C_1 is a complex constant. The CM can be either a phase-only mask with either greyscale (0 to 2π) or binary (0 or π) or a binary amplitude mask (0,1) that consists of pixels that can either block or allow light. The CM is given by a matrix $S_1 exp(iS_2)$, where S_1 is the magnitude component and S_2 is the phase component. When CM is a phase-only mask, S_1 becomes a matrix with a value of 1 at all pixels. When CM is an amplitude mask, S_2 has the same phase value at all the pixels. The complex amplitude after the CM is given as $\sqrt{I_s}C_1L\left(\frac{\bar{r}_s}{z_s}\right)Q\left(\frac{1}{z_s}\right)S_1 exp(iS_2)$, which is propagated by a distance z_h before reaching the image sensor. The intensity distribution of the point response recorded by the image sensor is given as

$$I_P(\bar{r}_0;\bar{r}_s,z_s) = \left|\sqrt{I_s}\,C_1L\left(\frac{\bar{r}_s}{z_s}\right)Q\left(\frac{1}{z_s}\right)S_1 exp(iS_2)\otimes Q\left(\frac{1}{z_h}\right)\right|^2 \tag{1}$$

where $\otimes$ stands for convolution and it is assumed that z_s and z_h are much longer than the CM size.

In a linear, shift-invariant system, the PSF can be expressed as

$$I_{PSF}(\bar{r}_0;z_s) = I_P\left(\bar{r}_0 - \frac{z_h}{z_s}\bar{r}_s;0,z_s\right) \tag{2}$$

Equation (2) indicates shift invariance where the intensity distribution on the sensor plane is a shifted version of the intensity response for a point object located on the optical axis $\bar{r}_s = 0$. The distance of the shift is $\frac{z_h}{z_s}\bar{r}_s$. For a 2D object O consisting of N points, the object can be expressed as a collection of delta functions

$$O(\bar{r}_s) = \sum_j^N a_j\delta\left(\bar{r}-\bar{r}_{s,j}\right) \tag{3}$$

where the j-th a_j is the amplitude of the respective point object labeled j. Considering the lack of spatial coherence, the light diffracted from two different points does not interact to form interference, but there is only an intensity addition given as

$$I_O(\bar{r}_0;z_s) = \sum_j^N a_j I_{PSF}\left(\bar{r}_0 - \frac{z_h}{z_s}\bar{r}_{s,j};z_s\right) \tag{4}$$

The object O can be reconstructed by processing I_{PSF} and I_O using one of the deconvolution methods. Recent studies have shown that LRRA and WD outperform the existing deconvolution methods and that INDIA can improve the final results of both LRRA and WD [31]. The initial input to the INDIA is crucial because it affects its output. A significant difference was observed in the performance of INDIA in choosing between the outputs of the NLR, LRA, LRRA, and WD as inputs of INDIA. Comparing LRRA and WD, LRRA generated higher values of SSIM (structural similarity index measure) than did WD. Here, we propose two improved versions of LRRA, NL-LRA1 and NL-LRA2, for two cases, namely, LSI and FVI. It is possible to convert FVI to LSI by zero padding, but when imaging multiplane objects consisting of several planes, it is

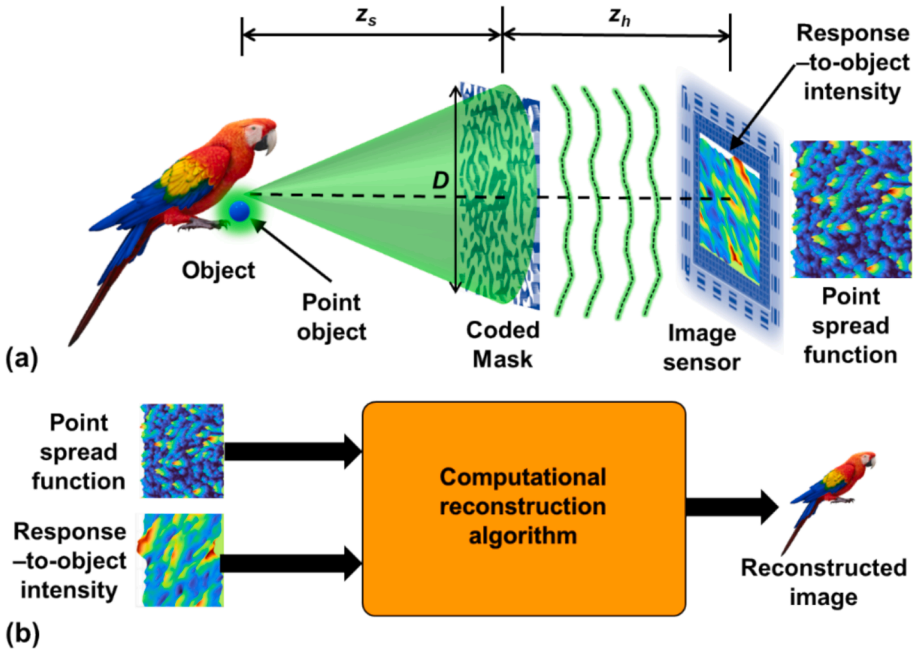

Fig. 1. (a) Optical configuration of the recording system and (b) computational reconstruction.

often challenging to discriminate background noise from background images to add accurate support. The $(n+1)^{th}$ reconstructed image of LRRA is given as

$$I_R^{n+1} = I_R^n \left\{ \left(\frac{I_O}{I_R^n \otimes I_{PSF}} \right) \circledast I_{PSF} \right\} \tag{5}$$

where I_R^n is defined below Eq. (6) and I_O is defined in Eq. (4). The symbol '$\circledast$' refers to the NLR, which is given as

$$A \circledast B = \mathscr{F}^{-1} \left\{ \left| \widetilde{A} \right|^{\alpha} exp\left[i \bullet arg\left(\widetilde{A} \right) \right] \left| \widetilde{B} \right|^{\beta} exp\left[-i \bullet arg\left(\widetilde{B} \right) \right] \right\}, \tag{6}$$

for two functions A and B where A is the PSF, B is the response-to-object intensity distribution, and $\widetilde{A}$ and $\widetilde{B}$ are the Fourier transforms of A and B, respectively. Schematics of NL-LRA1 and NL-LRA2 are shown in Figs. 2 and 3, respectively. NL-LRA1 is for the LSI. The algorithm begins with an initial guess of the solution ($I_R^{n=1}$), which is taken as I_O because this will make the algorithm work better and faster. Since I_O in many cases, such as when using an imaging lens as CM, is already close to the real solution, it speeds up the convergence rate and makes the process more stable. Setting I_O as the initial guess provides a better starting point and helps the algorithm find the solution more efficiently. If I_O is the solution, then $I_O \otimes I_{PSF}$ should yield I_O, which is not possible, but the ratio $= I_O/I_O$' yields valuable information on how far away the estimated solution is from the actual solution. This ratio is nonlinearly correlated with I_{PSF} to obtain the Fourier transform of the residue given as $\widetilde{Res}$ in Fig. 2. This magnitude of $\widetilde{Res}$ is multiplied by the previous solution $I_R^{n=1}$,

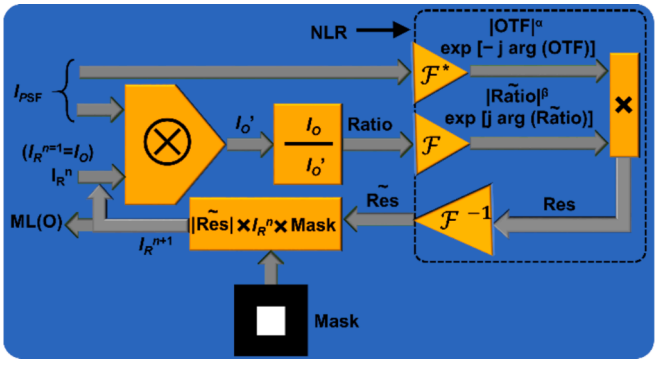

Fig. 2. Schematic of the NL-LRA1 algorithm. OTF – optical transfer function; n—number of iterations; $\otimes$ – 2D convolutional operator; I_R^n is the nth solution; and n is an integer; when $n = 1$, $I_R^n = I_O$; and α and β are varied from − 1 to 1; $\widetilde{\square}$ – Fourier transform of a variable; * – Complex conjugate of a variable; NLR is a nonlinear reconstruction; and $\mathscr{F}$ and $\mathscr{F}^{-1}$ are Fourier and inverse Fourier transforms, respectively; Res – Residue; and Mask is the magnitude constraint applied at every iteration.

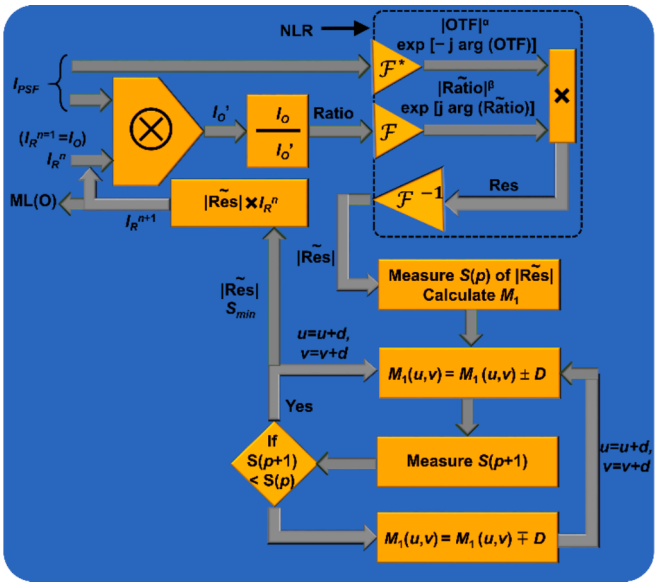

Fig. 3. Schematic of the NL-LRA2 algorithm. OTF – optical transfer function; n – number of iterations; $\otimes$ – 2D convolutional operator; I_R^n is the nth solution; and n is an integer; when $n = 1$, $I_R^n = I_O$; and α and β vary from −1 to 1; $\widetilde{\square}$ – Fourier transform of a variable; * – Complex conjugate of a variable; NLR is a nonlinear reconstruction; $\mathscr{F}$ and $\mathscr{F}^{-1}$ are Fourier and inverse Fourier transforms, respectively; Res – Residue; S is the entropy; M_1 is the matrix to minimize S; D is the increment applied to M_1; and p is the increment of the pixel location, which is used to control the sparsity of the search algorithm.

and by a matrix Mask that has ones within the area of the object and zeros elsewhere, to obtain the next solution $I_R^{n=2}$. The process is iterated until the solution converges to an optimal solution. In every iteration, the ratio arising from the inequality of $I_R^n \otimes I_{PSF} \neq I_O$ is converted into a correction term that is multiplied by the previous solution. In addition to this correction term, the multiplication of the mask with ones matched with the size of the object improves the correction in every iteration, enabling faster convergence. This seemingly meagre advancement improves the convergence speed nearly by 70 % with only one iteration for certain cases allowing the performance of non-iterative reconstruction algorithms to be reached (Supplementary Section 1).

NL-LRA2 is quite different from NL-LRA1, where the focus is on improving the performance of the NLR within the LRRA. In the INDIA, the performances of the NLR and any algorithm were improved based on the evidence that most of the object information is present in the phase of its spectrum. Therefore, by retaining this phase information and optimizing the magnitude of the spectrum with a magnitude constraint on the object size, the results were improved. However, the INDIA is not a blind method because it requires a metric such as the root mean squared error (RMSE) to measure the improvement at every iteration with respect to an ideal image. In NL-LRA2, once again, the phase of the spectrum is retained, but instead of the above approach of INDIA, the entropy of the output matrix of NLR is minimized blindly by changing the pixel values of the magnitude of the spectrum via a sparse search algorithm (SSA). Rewriting Eq. (6), after taking the Fourier transform on both sides, we obtain

$$\mathscr{F}(A \circledast B) = \left|\widetilde{A}\right|^{\alpha} exp\left[iarg\left(\widetilde{A}\right)\right]\left|\widetilde{B}\right|^{\beta} exp\left[-iarg\left(\widetilde{B}\right)\right] \tag{7}$$

In most of the studies [28–30], the optimal solution has been obtained when $\alpha = 0$ i.e., when only the phase of the spectrum of the PSF was used, so Eq. (7) can be modified to

$$\mathscr{F}(A \circledast B) = Mexp\left[iarg\left(\widetilde{A}\right)\right]exp\left[-iarg\left(\widetilde{B}\right)\right] \tag{8}$$

where $M = \left|\widetilde{B}\right|^{\beta}$. By solving for M, we obtain

$$M = \frac{\mathscr{F}(A \circledast B)}{exp\left[iarg\left(\widetilde{A}\right)\right]exp\left[-iarg\left(\widetilde{B}\right)\right]} = M_1 e^{i\theta} \tag{9}$$

In the first step, M is calculated from the phases of the spectrum and the output matrix $|A \circledast B|$ of the NLR. Only the magnitude M_1 of M is extracted, and the phase $e^{i\theta}$ is omitted because it is a weak function considering the formation of the NLR. At the beginning of the algorithm, the entropy $S(p = 0)$ of the output $|A \circledast B|$ is given as $S = -\sum_U \sum_V \phi(u,v) log[\phi(u,v)]$, where ϕ is the intensity normalized distribution function of the output of the NLR, which is $|A \circledast B|$. Single or multiple values are selected, and an array D is formed for the SSA. The pixel value $M_1(u,v)$ is incremented or decremented by the values of D, and for every change, the entropy $S(p = p + 1)$ is calculated and compared with $S(p)$. When the entropy is decreased, the change is retained, and if it is increased or remains unchanged, the pixel value is reverted to the previous value. Instead of doing the search pixel-by-pixel, a larger jump d can be selected to speed up the search process. In this way, by improving the NLR by entropy optimization given as NLR-EO, the solution of NL-LRA2 at every iteration is improved. There is a trade-off between obtaining the least S and the execution time. The greater the sparsity is, the lower the performance, and vice versa. Compared to NL-LRA1, NL-LRA2 can be considered blind because no partial information about the object, such as its size or location, is needed. The algorithm only focuses on reducing the entropy and improves the overall outcome of LRRA. In LRRA, NL-LRA1, and NL-LRA2, the parameters α and β are varied from -1 to 1 and do not change during the iteration process. In NL-LRA1, a simpler innovation of adding a limited support constraint within LRRA led to a significant improvement. In NL-LRA2, the innovation lies in the blind approach with a sparse search algorithm built within LRRA to minimize the entropy of the residue to achieve a high SNR. This improvement is carried forward to the object domain in the algorithm. The simulation studies carried out for extreme conditions of only one or two iterations show a significant improvement in NL-LRA2 compared with NLR, NLR-EO and LRRA (Supplementary Section 1).

The output from NL-LRA1 is fed into the INDIA, as shown in Fig. 4, which yields the best result. The INDIA was developed based on the assumption that most of the information of the object lies in the phase of the spectrum. Therefore, in the first step, the phase information of the blurred image and that of I_{PSF} are multiplied, and the spectral magnitude of NL-LRA1 is input. The resulting matrix is inverse Fourier transformed, and a magnitude constraint is applied while the phase information is carried forward. The resulting matrix is Fourier transformed, and the magnitude of the result replaces the previous one. This process is iterated until the output of the INDIA reaches a limit set by some figure of merit. The simulation studies are presented in Section 1 of the supplementary document.

3. Experimental studies

3.1. Optical experiments with visible light and spatial light modulator

Fig. 5(a) and 5(b) show a schematic and photograph of the optical experimental setup, respectively. In the setup, a high-power red LED (Element 1) from Thorlabs (940 mW, $\lambda = 660$ nm and $\Delta\lambda = 20$ nm) is used for illumination. The light illumination is controlled by an iris (Element 2). A diffuser (Element 3) from Thorlabs (Ø1″ Ground Glass Diffuser-220 GRIT) is used to remove the grating lines and control the noise emitted from the LED. The light from the diffuser is collimated by a refractive lens (Element 4) with a focal length of 5 cm. The collimated light enters the polarizer (Element 5) that is oriented along the active axis of the spatial light modulator (SLM) (Element 11) from Thorlabs (Exulus HD2, 1920 × 1200 pixels, pixel size = 8 μm). The light from the polarizer enters a refractive lens (Element 6) with a focal length of 5 cm that critically illuminates the pinhole/object (R1DS1N − Negative 1951 USAF Test Target, Ø1″) (Element 7). A pinhole of 50 μm and object digits '3′ and '1′ from Group (5) of the test target were used for this demonstration. The light from the pinhole/object is collimated using a refractive lens (Element 8) with a focal length of 5 cm. An iris (Element 9) is used to control the light illumination. The collimated light reaches the beam splitter (Element 10) and is incident on the SLM. The phase masks shown in Fig. 5(a) (row 1) were displayed one after the other on the SLM, and the corresponding I_{PSF} and I_O were recorded by an image sensor (Element 12) from Thorlabs (Zelux CS165MU/M 1.6 MP monochrome CMOS camera, 1440 × 1080 pixels, pixel size ~ 3.5 μm), which was placed at a distance of 17.8 cm from the SLM.

The experimental results for a single 'digit 3′ object are shown in Fig. 6 (a). Different phase-only CMs, such as a diffractive lens, diffractive axicon, cubic phase mask, quasi-random lens, and spiral axicon, were used for this study. Row 1 of Fig. 6 shows the phase images of the CMs: diffractive optical elements (DOEs) such as diffractive lens $exp\left[-i\pi\left(\lambda f\right)^{-1}R^2\right]$ where $R = \left(x^2 + y^2\right)^{1/2}$ with a maximum radius of 5 mm and focal length of $f = 20$ cm, diffractive axicon $exp\left[-i2\pi\Lambda^{-1}R\right]$ with period $\Lambda = 320$ μm, cubic phase mask $exp\left[-i(2\pi/\lambda)\left(ax^3 + by^3\right)\right]$ with $a = b \sim 1000$, quasi-random lens with a scattering ratio of $\sigma = 0.05$, and spiral axicon with $exp\left[-i2\pi\Lambda^{-1}R\right] \times exp[iL\theta]$ ($L = 5$ and $\Lambda = 320$ μm), where 'L' is the topological charge. The recorded I_{PSF} and I_O are shown in rows 2 and 3 of Fig. 6. The reconstruction results for I_R (NLR), I_R (LRRA), I_R (NL-LRA1), and I_R (INDIA), are shown in rows 4, 5, 6, and 7, respectively. A direct image of the object is shown at the bottom of Fig. 6 (a). As seen from the reconstruction results, the performance of NL-LRA1 is better than that of all the other reconstruction methods. We

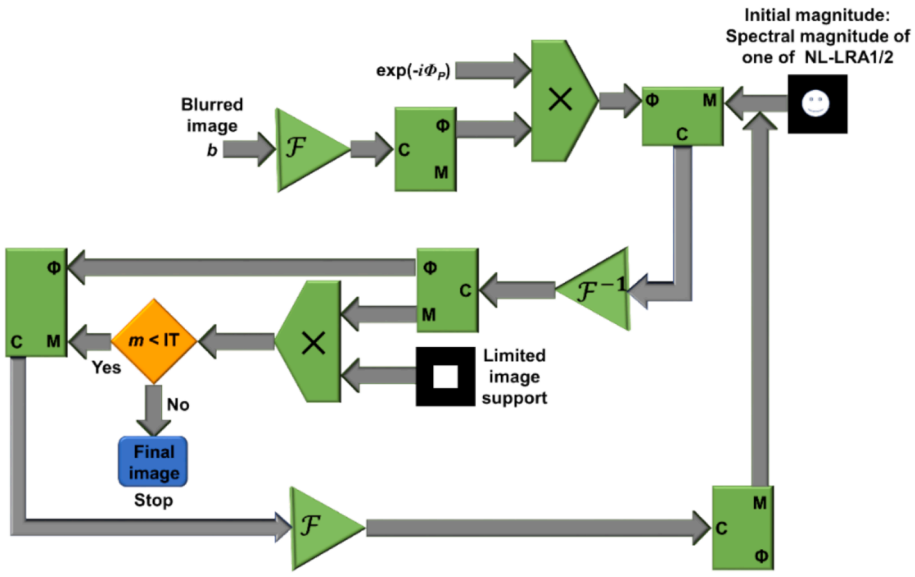

Fig. 4. Schematic of INDIA. C, Φ, and M are complex, phase and magnitude values, respectively; $\mathscr{F}$ and $\mathscr{F}^{-1}$ are Fourier and inverse Fourier transforms, respectively; IT is the threshold of the iteration number *m;* and $\exp(-i\Phi_P)$ is the conjugated phase of the PSF spectrum.

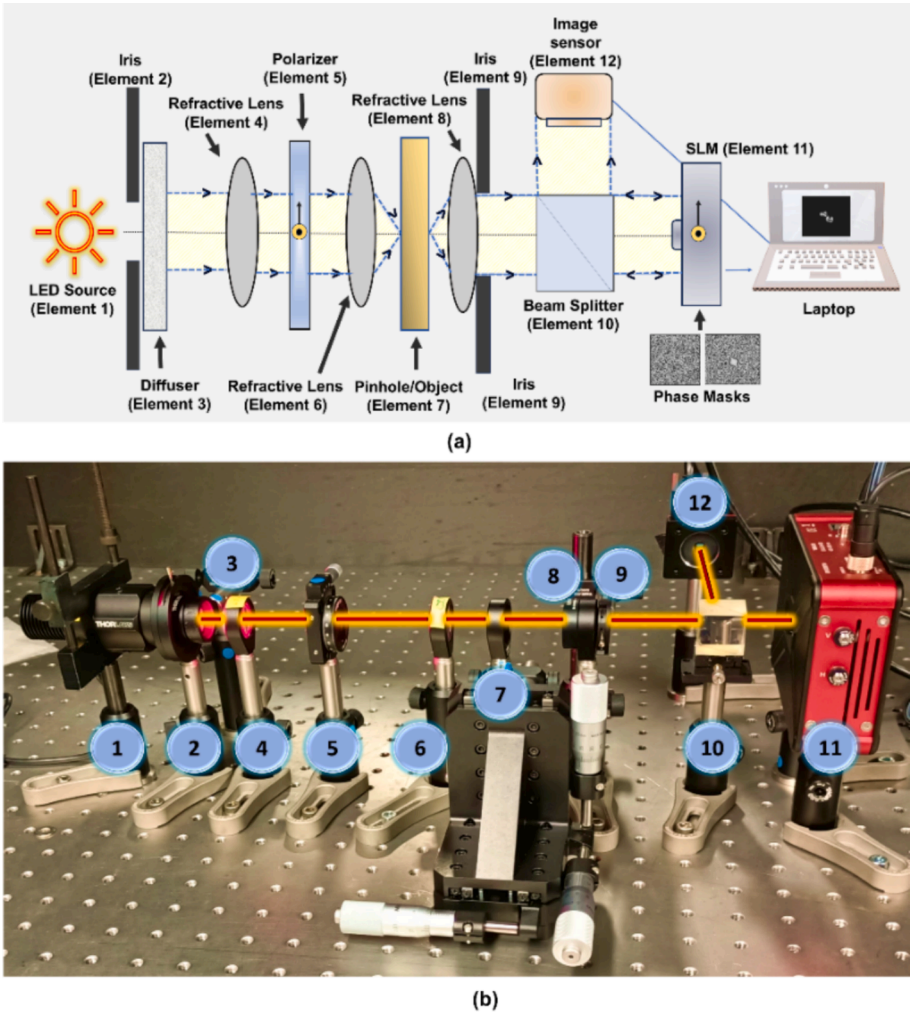

Fig. 5. (a) Schematic and (b) photograph of the experimental setup. (1) Red LED source, (2) iris, (3) diffuser, (4) refractive lens (f = 5 cm), (5) polarizer, (6) refractive lens (f = 5 cm), (7) pinhole/object, (8) refractive lens (f = 5 cm), (9) iris, (10) beam splitter, (11) SLM, (12) image sensor.

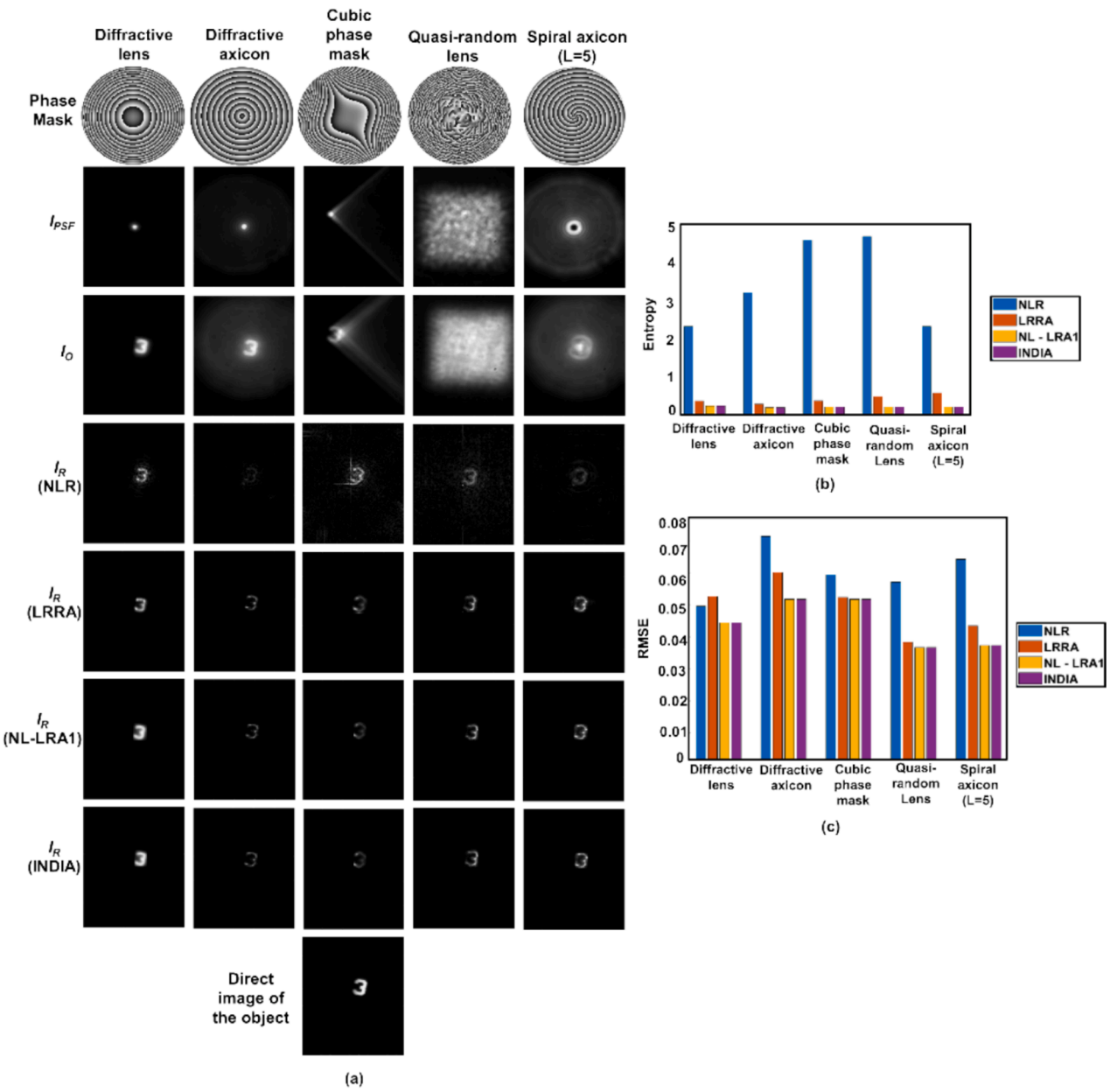

Fig. 6. (a) Row 1: Phase masks; Row 2: I_{PSF}; Row 3: I_O; Row 4: I_R (NLR); Row 5: I_R (LRRA); Row 6: I_R (NL-LRA1); Row 7: I_R (INDIA) for the diffractive lens, diffractive axicon, cubic phase mask, quasi-random lens and spiral axicon ($L = 5$). The direct image of the object is shown at the bottom. (b) The entropy and (c) RMSE plots for the diffractive lens, diffractive axicon, cubic phase, quasi-random lens, and spiral axicon ($L = 5$) correspond to Table 1 and Table 2.

Table 1
Entropy values of DOEs for different reconstruction methods.

DOEs /Reconstruction methods	Entropy			
	NLR	LRRA	NL-LRA1	INDIA
Diffractive lens	2.3041	0.3928	0.2616	0.2616
Diffractive axicon	3.1729	0.3869	0.2178	0.2178
Cubic phase mask	4.5269	0.4825	0.2388	0.2388
Quasi-random lens	4.6212	0.5009	0.2500	0.2500
Spiral axicon ($L = 5$)	3.6228	0.3458	0.2471	0.2471

Table 2
RMSE values of DOEs for different reconstruction methods.

DOEs /Reconstruction methods	RMSE			
	NLR	LRRA	NL-LRA1	INDIA
Diffractive lens	0.0497	0.0528	0.0446	0.0446
Diffractive axicon	0.0716	0.0563	0.0519	0.0519
Cubic phase mask	0.0596	0.0547	0.0516	0.0516
Quasi-random lens	0.0573	0.0385	0.0368	0.0368
Spiral axicon ($L = 5$)	0.0644	0.0436	0.0375	0.0375

calculated the entropy for the different CMs, as shown in Table 1, to quantify the results from all the reconstruction methods discussed. The entropy and RMSE plots corresponding to Table 1 and Table 2 are shown in Fig. 6 (b) and 6 (c). The plot shows that the entropy and RMSE are lowest for NL-LRA1, confirming the improvement of NL-LRA1 compared to the other reconstruction methods. Additionally, the performance of the INDIA is identical to that of the NL-LRA1. This is because the noise is not high in NL-LRA1, and the amplitude and phase information of NL-

LRA1 are fed as inputs to the INDIA. The typical ranges of the values of α and β and the number of iterations for LRRA and NL-LRA1 were 0 to 0.3, 1, and 6 to 10 iterations, respectively.

The experimental results for two digits '3′ and '1′, are shown in Fig. 7 (a). The recorded I_{PSF} and I_O are shown in rows 1 and 2 for the diffractive lens, diffractive axicon, cubic phase mask, quasi-random lens, and spiral axicon ($L = 5$), respectively. The reconstruction results for I_R (NLR), I_R (LRRA), and I_R (NL-LRA2) are shown in rows 3, 4, and 5 of Fig. 7(a), respectively. A direct image of the object is shown at the bottom of Fig. 7 (a). The entropy was calculated for the CMs, as shown in Table 3, to quantify the results of all the reconstruction methods discussed. The number of iterations used for the reconstruction methods LRRA and NL-LRA2 are shown in Table 4. The plots of entropy, number of iterations, and RMSE corresponding to Table 3, Table 4, and Table 5 are shown in Fig. 7(b), 7(c), and 7(d), respectively. From the results shown in Fig. 7 (a), the performance of NL-LRA2 is better than that of NLR and LRRA. As shown in Fig. 7(b), 7(c), and 7(d) NL-LRA2 has the lowest entropy and RMSE and requires fewer iterations than LRRA, which quantifies the results. As per our study results, in the case of other DOEs, the number of iterations required for NL-LRA2 is only half that of LRRA, and NL-LRA2 provides results with the least entropy and RMSE compared with NLR and LRRA. However, in the case of a diffractive lens, the number of iterations required for NL-LRA2 is the same as that for LRRA to obtain optimal results. In this scenario, the entropy is low, but the RMSE is slightly greater than that of LRRA, but it is lower than that of NLR.The major advantage of NL-LRA2 is that it can achieve the best results by entropy optimization blindly. However, NL-LRA2 might not benefit from having a shorter execution time, i.e., the number of iterations, because the time gained in reducing the number of iterations in LRRA is

Table 3
Entropy values of DOEs for different reconstruction methods.

DOEs/Reconstruction methods	Entropy		
	NLR	LRRA	NL-LRA2
Diffractive lens	3.4160	0.8507	0.8467
Diffractive axicon	3.2978	0.7568	0.6098
Cubic phase mask	3.9699	0.7493	0.6948
Quasi-random lens	5.0838	0.8018	0.7792
Spiral axicon ($L = 5$)	4.9073	0.8654	0.7794

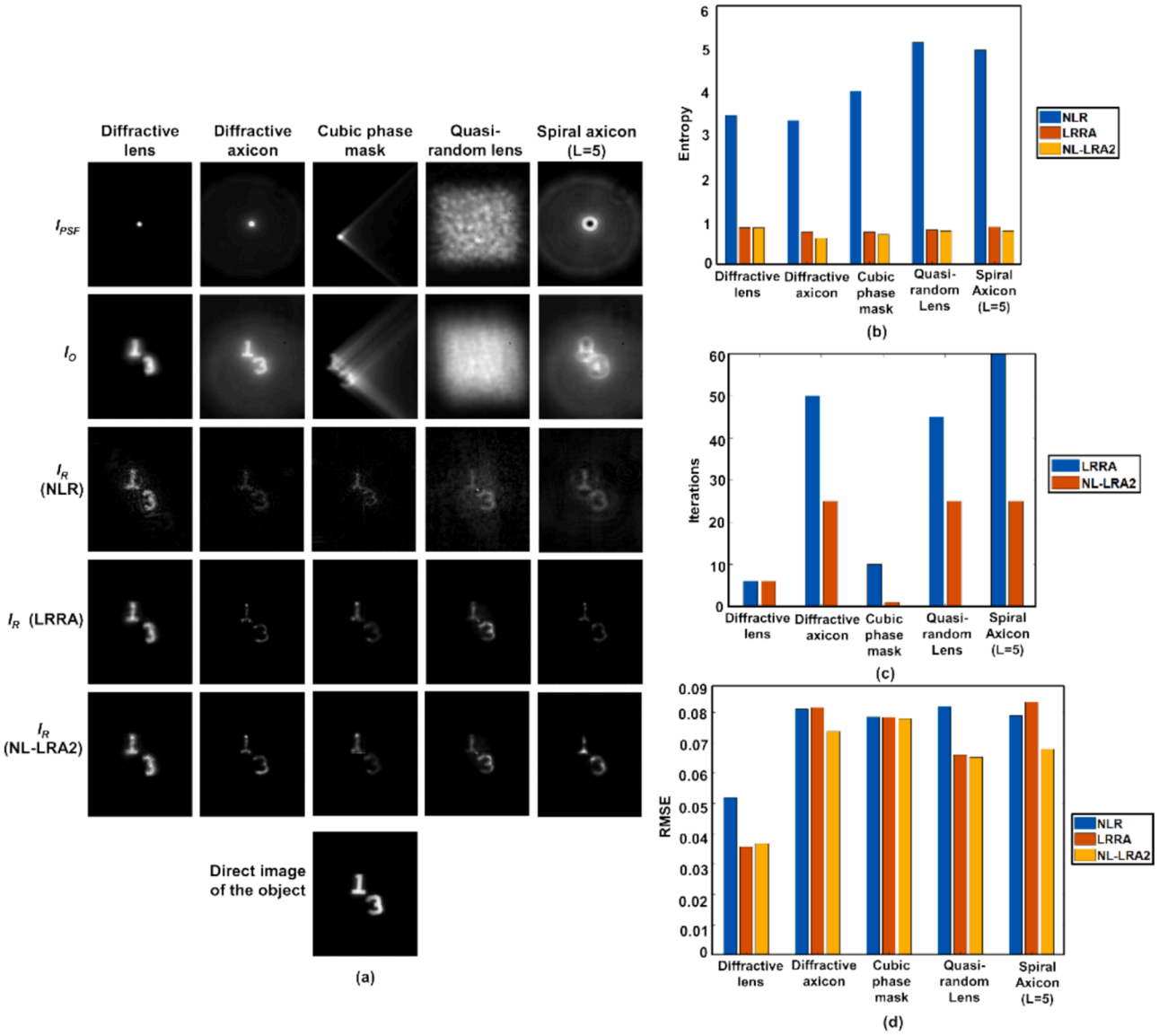

Fig. 7. (a) Row 1: I_{PSF}; Row 2: I_O; Row 3: I_R (NLR); Row 4: I_R (LRRA); Row 5: I_R (NL-LRA2) for the diffractive lens, diffractive axicon, cubic phase mask, quasi-random lens, and spiral axicon ($L = 5$). The direct image of the object is shown at the bottom. The plots of (b) entropy, (c) number of iterations, and (d) RMSE for the diffractive lens, diffractive axicon, cubic phase, quasi-random lens, and spiral axicon (L = 5) correspond to Table 3, Table 4, and Table 5 respectively.

Table 4
Iteration values of DOEs for LRRA and NL-LRA2.

DOEs/Reconstruction methods	Number of iterations	
	LRRA	NL-LRA2
Diffractive lens	6	6
Diffractive axicon	50	25
Cubic phase mask	10	1
Quasi-random lens	45	25
Spiral axicon ($L = 5$)	60	25

Table 5
RMSE values of DOEs for different reconstruction methods.

DOEs /Reconstruction methods	RMSE		
	NLR	LRRA	NL-LRA2
Diffractive lens	0.0778	0.0357	0.0368
Diffractive axicon	0.0810	0.0816	0.0737
Cubic phase mask	0.0784	0.0783	0.0779
Quasi-random lens	0.0819	0.0702	0.0677
Spiral axicon ($L = 5$)	0.0789	0.0834	0.0679

almost utilized during entropy optimization. Therefore, the main advantage is the better SNR measured by reduced entropy. The typical ranges of the values of α and β and the number of iterations for LRRA are 0.1 to 0.3, 1, and 6 to 60 iterations. For NL-LRA2, α, β, and the number of iterations were 0.1 to 0.3, 1, and 5 to 25 iterations. The execution time of NL-LRA2 depends upon the number of iterations used and the number of variables checked in the algorithm. For example, the maximum number of iterations used in this study is 25, with a sparsity defined by a pixel jump of 10 pixels. There is a trade-off between computational cost and entropy. A sparse search reduces the computational cost at the expense of a slight increase in the entropy.

3.2. Optical experiments with IR light

3.2.1. Experiments

The schematic of experimental configuration using IR light is shown in Fig. 8(a). The DOEs fabrication procedure is presented in the section 2 of the supplementary document. The photograph of the experimental setup is shown in Fig. 8(b). In the setup, the IR light is emitted from the source (Thorlabs SLS303, $\lambda = 550$ nm-15 μm) (Element 1) with a power controller (Element 2), and the light illumination is controlled using an iris (Element 3). A concave mirror (Thorlabs CM254-100-P01) (Element 4) is used to critically illuminate the pinhole (200 μm) (Element 6). An iris (Element 5) is placed in front of the pinhole to control light illumination. The light from the pinhole is collimated using a plano-convex lens (Edmund Optics 50 mm Dia. × 100 mm FL uncoated calcium fluoride PCX lens) (Element 7). The collimated light is controlled by another iris (Element 8) and is incident on the fabricated DOE (Element 9). The DOEs (diffractive axicon, cubic phase mask, and quasi-random lens) were placed one after the other, and the holograms were recorded using an IR camera (FLIR A 6700, 640 × 512 arrays with 15 μm pixel size, operating range: 1–5 μm) (Element 10). The distance between the IR source and the pinhole was 27 cm, and the distance between the pinhole and the fabricated DOE was 35 cm. The IR camera was placed at a distance of 4 cm from the DOEs. In this experiment, two points were used as the object (each with a size of 200 μm) and were recorded by shifting the pinhole at two different locations. The distance between the two points was 2 mm.

The experimental results for two points are shown in Fig. 8(c). The recorded I_{PSF} and I_O are shown in columns 1 and 2, and the reconstruction results for I_R (NLR), I_R (LRRA), and I_R (NL-LRA2) are shown in columns 3, 4, and 5 for the diffractive axicon, cubic phase mask, and

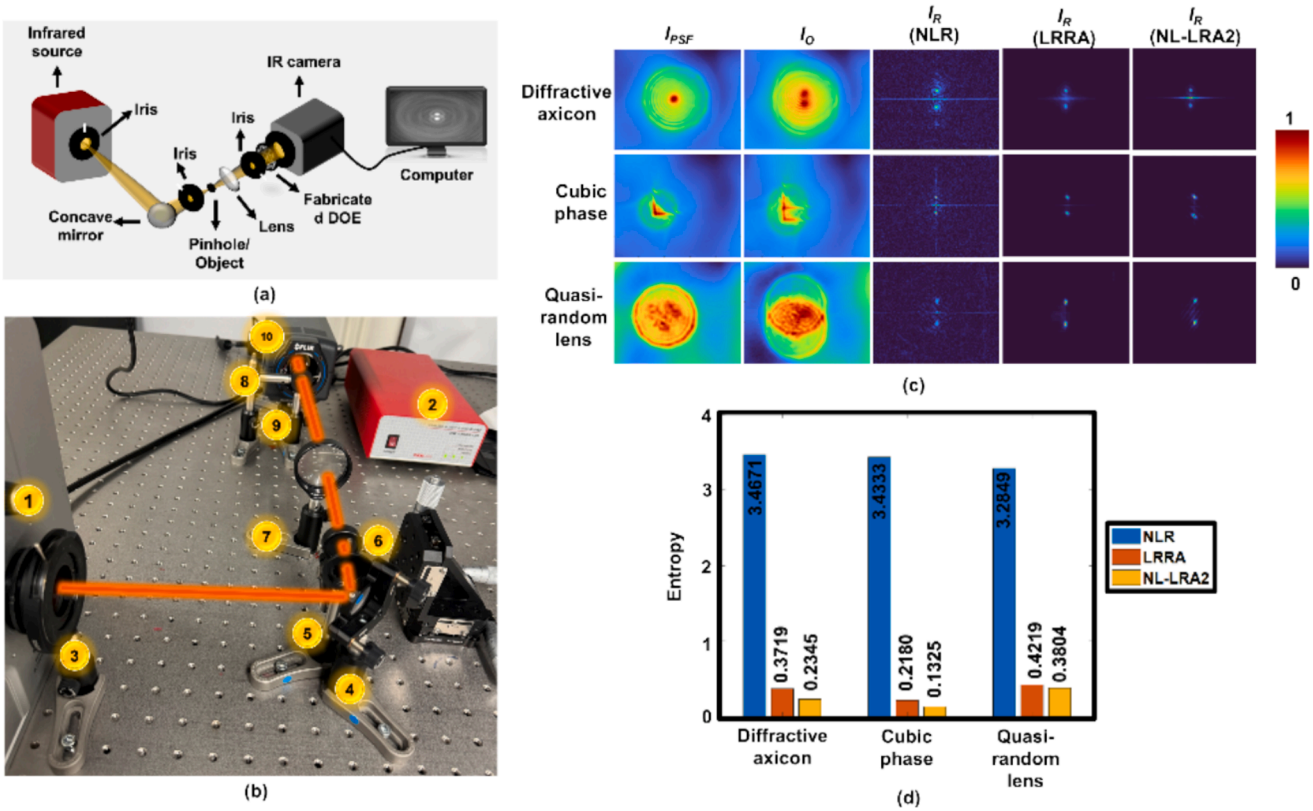

Fig. 8. (a) Schematic and (b) photograph of the experimental setup for IR imaging. (1) IR source, (2) power controller, (3) iris, (4) concave mirror, (5) iris, (6) pinhole (200 μm), (7) plano-convex lens (f = 10 cm), (8) iris, (9) DOE, (10) IR camera. (c) column 1: IPSF; column 2: IO; column 3: IR (NLR); column 4: IR (LRRA); and column 5: IR (NL-LRA2). (d) Entropy plots for the diffractive axicon, cubic phase mask, and quasi-random lens.

quasi-random lens, respectively. The entropy plot is shown in Fig. 8(d). The typical ranges of α and β for the NLR, LRRA, and NL-LRA2 were 0 to 0.4 and 0.1 to 1, respectively. The number of iterations of LRRA for the diffractive axicon, cubic phase mask, and quasi-random lens are 12, 8, and 7, respectively. Similarly, the number of iterations of NL-LRA2 for the diffractive axicon, cubic phase mask, and quasi-random lens are 10, 7, and 7, respectively. According to the results, the performance of NL-LRA2 is better than that of LRRA in terms of entropy and the number of iterations.

3.2.2. *Optical experiments with a commercial laboratory-based internal IR light source and synchrotron IR radiation*

To further analyze the performance of NL-LRA2, we assessed its potential for IR imaging applications on experimental data recorded from a commercial IR microscope equipped with an internal Globar™ broadband IR light source (Bruker Optik GmbH, Ettlingen, Germany). This IR microscope uses reflective Cassegrain objective lenses that generate unique 3D PSFs characterized by the four lobes [28]. The I_{PSF}s (25 μm pinhole) and response-to-object intensity distributions for two test objects, including a cross-shaped object (150 μm × 150 μm) and a random pinhole object (50 μm in diameter), ablated on a chromium-gold-coated calcium fluoride substrate were recorded at the same depth. The experimental results are shown in Fig. 9(a) for cross-shaped object and random pinhole object. The recorded IR direct image, I_{PSF}, I_O, I_R (NLR), I_R (LRRA), and I_R (NL-LRA2) are shown in columns 1, 2, 3, 4, 5, and 6 for cross-shaped and random pinhole objects, respectively. The typical ranges of α and β for the NLR, LRRA, and NL-LRA2 were 0 to 0.5 and 0.6 to 1, respectively. The number of iterations of LRRA for cross-shaped and random pinhole objects was 40 and 17, respectively. Similarly, the number of iterations of NL-LRA2 for cross-shaped and random pinhole objects was 25 and 14, respectively. The entropy plot is shown in Fig. 9(c). Compared with that of LRRA, the entropy of NL-LRA2 decreases as the number of iterations decreases. Once again, from the entropy plot and number of iterations, we confirm that the performance of NL-LRA2 is better than that of LRRA for both cross-shaped and random pinhole objects.

We extended our experimental study of NL-LRA2 by recording data from an IR microscope that used synchrotron IR radiation as an IR light source at the Australian Synchrotron's Infrared Microspectroscopy (IRM) beamline (Clayton, Victoria). Instead of Cassegrain objective pairs, the reflective Schwarzschild objective lens pair is characterized by a unique I_{PSF} with three lobes, as shown in Fig. 9(b). The above-mentioned cross-shaped test object was again used for these experiments. The experimental results are shown in Fig. 9(b). The imaging results obtained using I_{PSF}, I_O, I_R (NLR), I_R (LRRA), and I_R (NL-LRA2) are shown from left to right, respectively. The entropy plot is shown in Fig. 9 (d). The typical ranges of α and β for the NLR, LRRA, and NL-LRA2 were 0.1 to 0.3 and 0.3 to 1, respectively. The number of iterations used for LRRA and NL-LRA2 is 6. In this case, within a short period, NL-LRA2 provides the best result, i.e., with minimum entropy due to the smaller number of iterations compared to the other reconstruction methods.

3.3. *Experiments with a smart phone camera*

To verify the performance of the proposed algorithm in practical applications where measuring or recording I_{PSF} is challenging, we imaged complex natural objects, i.e., a leaf and scenery using a smartphone camera with a low F-number (iPhone 15 Pro Max, 48-megapixel, f/1.8 primary camera) and reconstructed them using synthetic I_{PSF}s. We

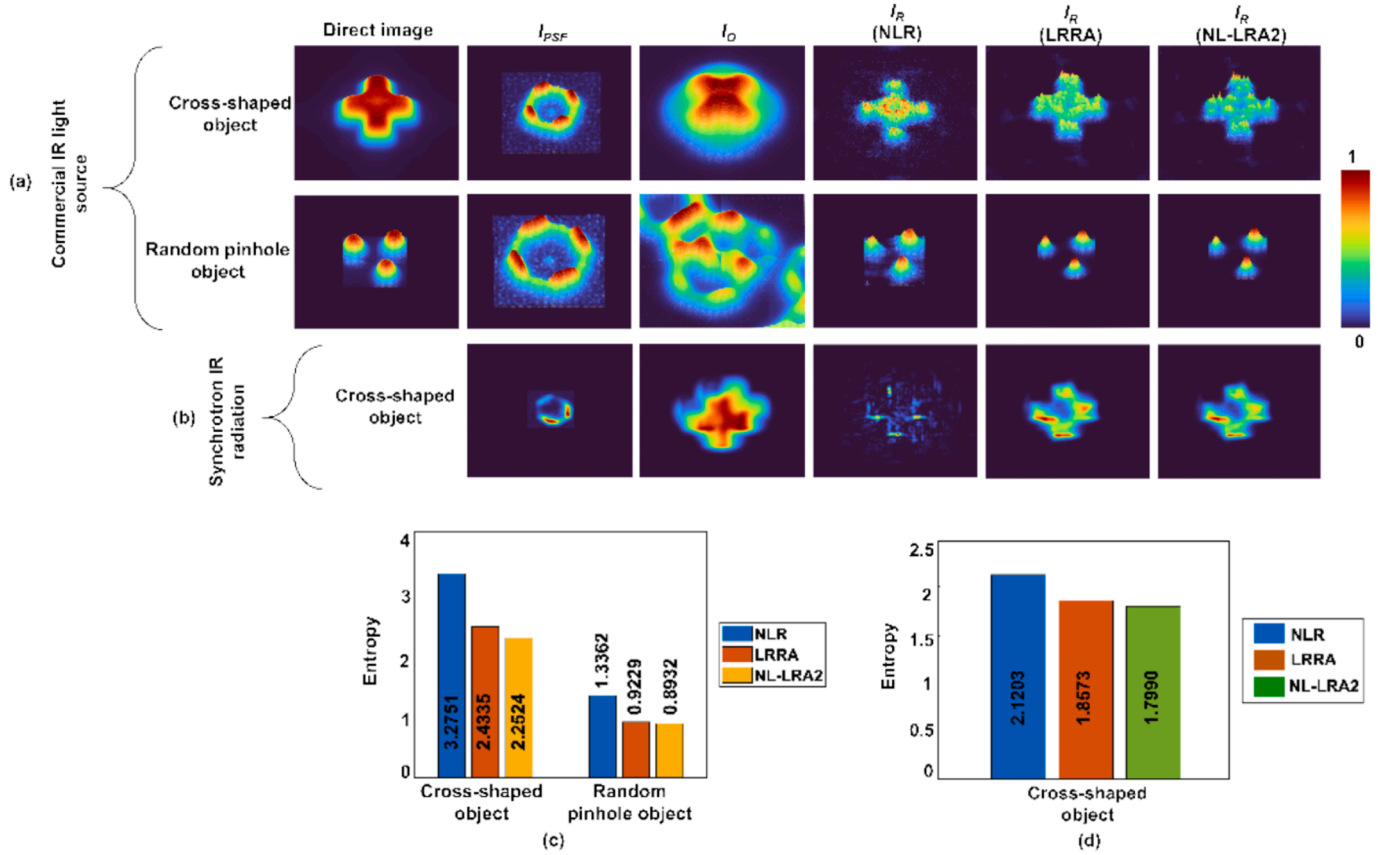

Fig. 9. (a) Commercial IR light source – Column 1: Direct image of the object; column 2: I_{PSF}; column 3: I_O; column 4: I_R (NLR); column 5: I_R (LRRA); column 6: I_R (NL-LRA2); and (c) entropy plot for the cross-shaped object and random pinhole object. (b) Synchrotron IR radiation – From left to right: I_{PSF}, I_O, I_R (NLR), I_R (LRRA), and I_R (NL-LRA2) and (d) entropy plots for the cross-shaped object.

recorded the two objects using a low F-number setting of the smartphone, resulting in blurred images. Then, we synthesized the PSFs and applied the NL-LRA2 algorithm, as the recorded images are FVIs. We compared the results with the results from other reconstruction methods. The results are shown in Fig. 10. The number of iterations used for LRRA and NL-LRA2 are 7 for natural object 1 (leaf) and 6 for natural object 2 (scenery). The typical ranges of α and β for the NLR, LRRA, and NL-LRA2 were 0–0.9 and 0.9–1, respectively. The entropy plot is shown in Fig. 10(s). In this experimental setting, the blur is well understood and weak, unlike complicated methods with different phase masks, and therefore, all the reconstruction methods are expected to perform well. However, even with this minimally blurry case, NL-LRA2 provides a better reconstruction result with the least entropy compared with LRRA and other reconstruction methods.

4. Conclusion

Two image reconstruction algorithms, NL-LRA1 and NL-LRA2, for LSI and FVI have been developed. NL-LRA1 uses a mask constraint to increase the convergence speed of the algorithm and provides a better estimation of the solution. NL-LRA2 uses an internal entropy minimization method using a sparse search method to find the magnitude of the spectrum that will render a minimum entropy without altering the phase of the spectrum. The speed of NL-LRA1 is the same as that of LRRA in all cases for every iteration, but the number of iterations required for NL-LRA1 is lower than that of LRRA, and most importantly, NL-LRA1 yields better reconstruction results. The speed of NL-LRA2 is slower than that of LRRA. In LRRA, the speed depends only on the number of iterations used, but in NL-LRA2, the speed depends on the number of iterations, the number of pixel jumps, the matrix size used, and the number of variables checked in the algorithm. Additionally, it depends on the complexity of the image. In most cases, the optimal results will be obtained with fewer iterations where the execution time is faster, and in some instances, the optimal result will be obtained only with a greater number of iterations where the execution time is slower. Even though NL-LRA2 requires more execution time than LRRA does, it yields better results than NLR and LRRA do with fewer iterations, so the penalty is not high. Both the NL-LRA1 and NL-LRA2 algorithms were tested in CAI using different light sources, (i.e. visible light, IR light, and synchrotron IR radiation), different imaging systems, (i.e. CAI and commercial IR microscopy), with various CMs, (i.e. phase-only diffractive masks and amplitude-type diffractive masks) and reflective objectives, (i.e. Cassegrain and Schwarzschild objectives). The results of the new methods were compared with those of their parent methods, NLR and LRRA, and it was confirmed that the new methods offer an improved SNR compared to that of the parent methods. From the experimental studies, we

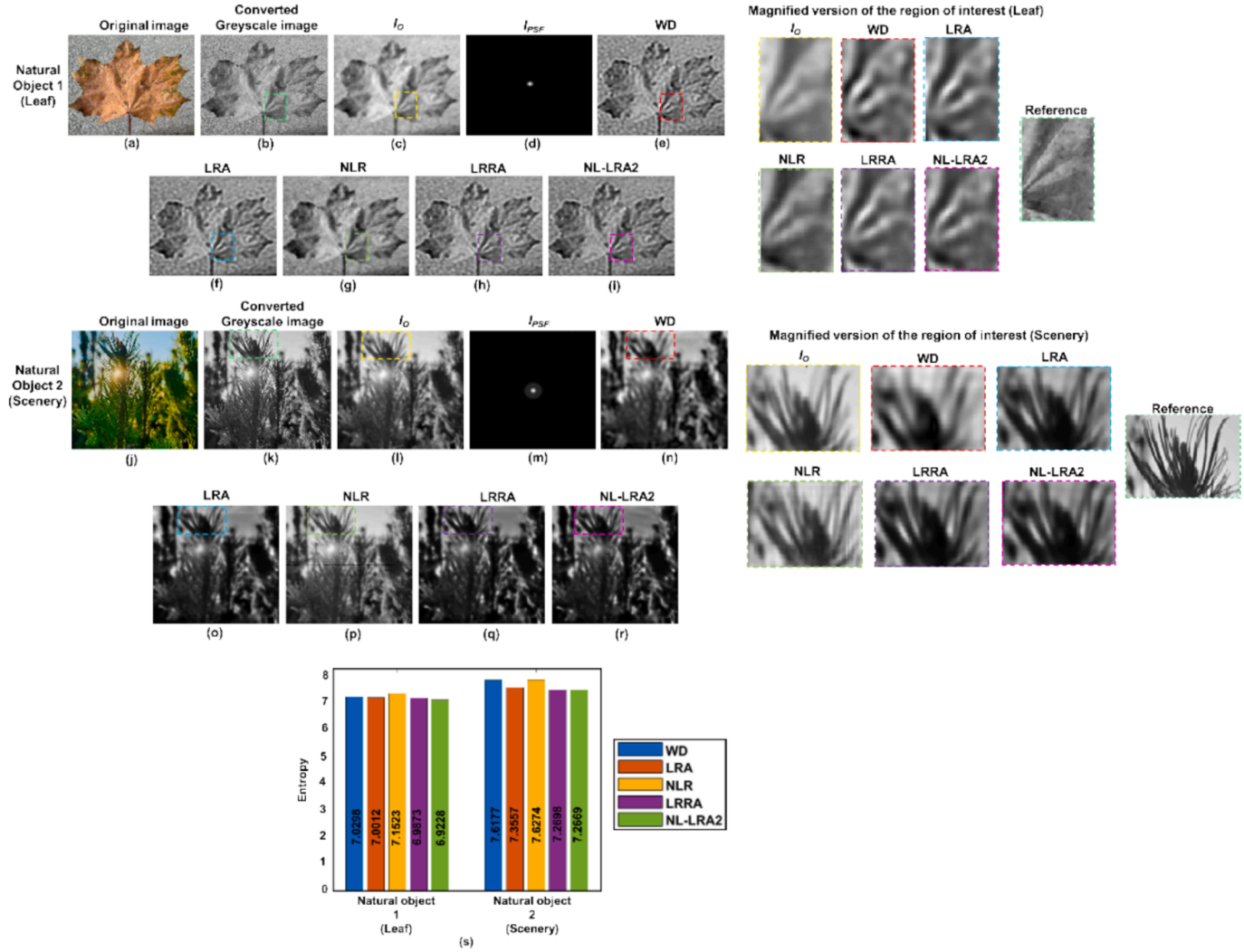

Fig. 10. Natural object 1 (Leaf): (a) original image, (b) converted greyscale image, (c) I_O, (d) I_{PSF}, reconstruction results by (e) WD (f) LRA, (g) NLR, (h) LRRA and (i) NL-LRA2. Natural object 2 (Scenery): (j) original image, (k) converted greyscale image, (l) I_O, (m) I_{PSF}, reconstruction results by (n) WD (o) LRA, (p) NLR, (q) LRRA and (r) NL-LRA2. (s) Entropy plot for natural objects 1 (leaf) and 2 (scenery).

analyzed that NL-LRA1 performs well for LSIs and that NL-LRA2 performs well for FVIs in different circumstances. In conclusion, NL-LRA1 and NL-LRA2 were developed to improve image recovery in two directions, namely, time and image quality, with minimal entropy. Based on the study using diverse data, we believe that the development of NL-LRA1 and NL-LRA2 will have a significant impact on image recovery, as the developed iterative algorithms perform as fast as non-iterative algorithms do, requiring only 1–2 iterations for many scenarios. We strongly believe that NL-LRA1 and NL-LRA2 will set a new benchmark for image recovery of LSIs and FVIs and that they will potentially be applicable in fields such as computational imaging, incoherent digital holography, CAI, live-cell imaging, computed tomography, high-speed imaging and IR imaging.

CRediT authorship contribution statement

Agnes Pristy Ignatius Xavier: Writing – review & editing, Writing – original draft, Validation, Software, Formal analysis, Data curation. **Tauno Kahro:** Writing – review & editing, Writing – original draft, Validation, Software, Resources, Data curation. **Shivasubramanian Gopinath:** Writing – review & editing, Writing – original draft, Validation, Software, Data curation. **Vipin Tiwari:** Writing – review & editing, Validation, Software, Data curation. **Daniel Smith:** Writing – review & editing, Validation, Software. **Aarne Kasikov:** Writing – review & editing, Validation, Software, Resources. **Helle-Mai Piirsoo:** Writing – review & editing, Validation, Software, Resources, Data curation. **Soon Hock Ng:** Writing – review & editing, Validation, Software, Resources, Data curation. **Aravind Simon John Francis Rajeswary:** Writing – review & editing, Validation, Software. **Jitraporn Vongsvivut:** Writing – review & editing, Validation, Software, Resources, Funding acquisition. **Aile Tamm:** Writing – review & editing, Validation, Supervision, Software, Resources, Project administration, Funding acquisition. **Kaupo Kukli:** Writing – review & editing, Validation, Supervision, Software, Resources, Project administration, Funding acquisition. **Saulius Juodkazis:** Writing – review & editing, Visualization, Validation, Supervision, Software, Resources, Investigation, Funding acquisition, Formal analysis. **Joseph Rosen:** Writing – review & editing, Writing – original draft, Visualization, Validation, Supervision, Software, Resources, Methodology, Investigation, Funding acquisition, Formal analysis, Data curation, Conceptualization. **Vijayakumar Anand:** Writing – review & editing, Writing – original draft, Visualization, Validation, Supervision, Software, Resources, Project administration, Methodology, Investigation, Funding acquisition, Formal analysis, Data curation, Conceptualization.

Funding

Israel Innovation Authority (79555, MAGNET); Horizon 2020 Framework Programme (857627, CIPHR); NAMUR + core facility funded by the Estonian Research Council (TT 13); Discovery Grant DP240103231 from Australian Research Council. The synchrotron IR experiments were performed on the IRM beamline at the Australian Synchrotron, part of ANSTO, through merit-based access (Proposal ID. 20635).

Declaration of competing interest

The authors declare that they have no known competing financial interests or personal relationships that could have appeared to influence the work reported in this paper.

Appendix A. Supplementary material

The simulation results and the fabrication procedure are given in the supplementary document. Commented MATLAB codes for executing NL-LRA1 and NL-LRA2 are provided as text files.

Supplementary data to this article can be found online at https://doi.org/10.1016/j.optlastec.2024.112300.

Data availability

Data will be made available on request.

References

[1] J.G. Ables, Fourier transform photography: a new method for X-ray astronomy, Publ. Astron. Soc. Aust. 1 (1968) 172–173.
[2] R.H. Dicke, Scatter-hole cameras for X-rays and gamma rays, Astrophys. J. 153 (1968). L101 L106.
[3] E.E. Fenimore, T.M. Cannon, Coded aperture imaging with uniformly redundant arrays, Appl. Opt. 17 (1978) 337–347.
[4] M.J. Cieslak, K.A.A. Gamage, R. Glover, Coded-aperture imaging systems: past, present and future development–a review, Radiat. Meas. 92 (2016) 59–71.
[5] J.Y. Liang, Punching holes in light: recent progress in single-shot coded-aperture optical imaging, Rep. Prog. Phys. 83 (2020) 116101.
[6] B. Javidi, A. Carnicer, A. Anand, G. Barbastathis, W. Chen, et al., Roadmap on digital holography, Opt. Express 29 (2021) 35078–35118.
[7] J. Rosen, A. Vijayakumar, M. Kumar, M.R. Rai, R. Kelner, Y. Kashter, A. Bulbul, S. Mukherjee, Recent advances in self-interference incoherent digital holography, Adv. Opt. Photon. 11 (2019) 1–66.
[8] T. Tahara, Y. Zhang, J. Rosen, V. Anand, L. Cao, J. Wu, T. Koujin, A. Matsuda, A. Ishii, Y. Kozawa, R. Okamoto, T. Nobukawa, K. Choi, M. Imbe, T. Poon, Roadmap of incoherent digital holography, Appl. Phys. B 128 (2022) 193.
[9] E.E. Fenimore, Coded aperture imaging: predicted performance of uniform redundant arrays, Appl. Opt. 17 (1978) 3562–3569.
[10] S.R. Gottesman, E.E. Fenimore, New family of binary arrays for coded aperture imaging, Appl. Opt. 28 (1989) 4344–4352.
[11] H.H. Barrett, W.W. Stoner, D.T. Wilson, G.D. DeMeester, Coded apertures derived from the Fresnel zone plate, Opt. Eng. 13 (1974) 122–136.
[12] J.L. Horner, P.D. Gianino, Phase-only matched filtering, Appl. Opt. 23 (1984) 812–816.
[13] G.M. Robbins, T.S. Huang, Inverse filtering for linear shift-variant imaging systems, Proc. IEEE 60 (1972) 862–872.
[14] A. Dhawan, R. Rangayyan, R. Gordon, Image restoration by Wiener deconvolution in limited-view computed tomography, Appl. Opt. 24 (1985) 4013–4020.
[15] W. Richardson, Bayesian-based iterative method of image restoration, J. Opt. Soc. of Am. 62 (1972) 55–59.
[16] L.B. Lucy, An iterative technique for the rectification of observed distributions, Astron. J. 79 (1974) 745–754.
[17] A. Wagadarikar, R. John, R. Willett, D. Brady, Single disperser design for coded aperture snapshot spectral imaging, Appl. Opt. 47 (2008) B44–B51.
[18] S.K. Sahoo, D. Tang, C. Dang, Single-shot multispectral imaging with a monochromatic camera, Optica 4 (2017) 1209–1213.
[19] A. Vijayakumar, J. Rosen, Interferenceless coded aperture correlation holography–a new technique for recording incoherent digital holograms without two-wave interference, Opt. Express 25 (2017) 13883–13896.
[20] M.R. Rai, A. Vijayakumar, Y. Ogura, J. Rosen, Resolution enhancement in nonlinear interferenceless COACH with point response of subdiffraction limit patterns, Opt. Express 27 (2019) 391–403.
[21] M.R. Rai, A. Vijayakumar, J. Rosen, Extending the field of view by a scattering window in an I-COACH system, Opt. Lett. 43 (2018) 1043–1046.
[22] A. Bulbul, A. Vijayakumar, J. Rosen, Partial aperture imaging by systems with annular phase CM, Opt. Express 25 (2017) 33315–33329.
[23] M.R. Rai, J. Rosen, Depth-of-field engineering in coded aperture imaging, Opt. Express 29 (2021) 1634–1648.
[24] S. Mukherjee, A. Vijayakumar, J. Rosen, Spatial light modulator aided noninvasive imaging through scattering layers, Sci Rep 9 (2019) 17670.
[25] M.R. Rai, A. Vijayakumar, J. Rosen, Non-Linear adaptive three dimensional imaging with interferenceless coded aperture correlation holography (I-COACH), Opt. Express 26 (2018) 18143–18154.
[26] Y. Wan, C. Liu, T. Ma, Y. Qin, S. lv, Incoherent coded aperture correlation holographic imaging with fast adaptive and noise-suppressed reconstruction, Opt. Express 29 (2021) 8064–8075.
[27] M. Zhang, Y. Wan, T. Man, W. Zhang, H. Zhou, Non-iterative reconstruction of interferenceless coded aperture correlation holography enabled high quality three-dimensional imaging, Opt. Lasers Eng. 173 (2024) 107929.
[28] V. Anand, M. Han, J. Maksimovic, S.H. Ng, T. Katkus, A. Klein, K. Bambery, M. J. Tobin, J. Vongsvivut, S. Juodkazis, Single-shot mid-infrared incoherent holography using Lucy-Richardson-Rosen algorithm, Opto-Electron. Sci. 1 (2022) 210006.
[29] A.P.I. Xavier, F.G. Arockiaraj, S. Gopinath, et al., Single shot 3D incoherent imaging using deterministic and random optical fields with Lucy-Richardson-Rosen algorithm, Photonics 10 (2023) 987.
[30] P.A. Praveen, F.G. Arockiaraj, S. Gopinath, et al., Deep deconvolution of object information modulated by a refractive lens using Lucy-Richardson-Rosen algorithm, Photonics 9 (2022) 625.
[31] J. Rosen, V. Anand, Incoherent nonlinear deconvolution using an iterative algorithm for recovering limited-support images from blurred digital photographs, Opt. Express 32 (2024) 1034–1046.

[32] Q. Zhang, T. Huang, J. Li, et al., Single-shot deep-learning based 3D imaging of Fresnel incoherent correlation holography, Opt. Lasers Eng. 172 (2024) 107869.
[33] Y. Wang, H. Wang, S. Liu, et al., Unsupervised deep learning enables 3D imaging for single-shot incoherent holography, Laser Photonics Rev. (2024) 2301091.
[34] H. Yu, Y. Kim, D. Yang, et al., Deep learning-based incoherent holographic camera enabling acquisition of real-world holograms for holographic streaming system, Nat. Commun. 14 (2023) 3534.